



Improved Characterization of the Astrophysical Muon–neutrino Flux with 9.5 Years of IceCube Data

R. Abbasi¹, M. Ackermann², J. Adams³, J. A. Aguilar⁴, M. Ahlers⁵, M. Ahrens⁶, J. M. Alameddine⁷, C. Alispach⁸, A. A. Alves Jr.⁹, N. M. Amin¹⁰, K. Andeen¹¹, T. Anderson¹², G. Anton¹³, C. Argüelles¹⁴, Y. Ashida¹⁵, S. Axani¹⁶, X. Bai¹⁷, A. Balagopal V.¹⁵, A. Barbano⁸, S. W. Barwick¹⁸, B. Bastian², V. Basu¹⁵, S. Baur⁴, R. Bay¹⁹, J. J. Beatty^{20,21}, K.-H. Becker²², J. Becker Tjus²³, C. Bellenghi²⁴, S. BenZvi²⁵, D. Berley²⁶, E. Bernardini^{27,62}, D. Z. Besson²⁸, G. Binder^{19,28}, D. Bindig²², E. Blaufuss²⁶, S. Blot², M. Boddenberg²⁹, F. Bontempo⁹, J. Borowka²⁹, S. Böser³⁰, O. Botner³¹, J. Böttcher²⁹, E. Bourbeau⁵, F. Bradascio², J. Braun¹⁵, B. Brinson³², S. Bron⁸, J. Brostean-Kaiser², S. Browne³³, A. Burgman³¹, R. T. Burley³⁴, R. S. Busse³⁵, M. A. Campana³⁶, E. G. Carnie-Bronca³⁴, C. Chen³², Z. Chen³⁷, D. Chirkin¹⁵, K. Choi³⁸, B. A. Clark³⁹, K. Clark⁴⁰, L. Classen³⁵, A. Coleman¹⁰, G. H. Collin¹⁶, J. M. Conrad¹⁶, P. Coppin⁴¹, P. Correa⁴¹, D. F. Cowen^{12,42}, R. Cross²⁵, C. Dappen²⁹, P. Dave³², C. De Clercq⁴¹, J. J. DeLaunay⁴³, D. Delgado López¹⁴, H. Dembinski¹⁰, K. Deoskar⁶, A. Desai¹⁵, P. Desiati¹⁵, K. D. de Vries⁴¹, G. de Wasseige⁴⁴, M. de With⁴⁵, T. DeYoung³⁹, A. Diaz¹⁶, J. C. Díaz-Vélez¹⁵, M. Dittmer³⁵, H. Dujmovic⁹, M. Dunkman¹², M. A. DuVernois¹⁵, E. Dvorak¹⁷, T. Ehrhardt³⁰, P. Eller⁴⁰, R. Engel^{9,33}, H. Erpenbeck²⁹, J. Evans²⁶, P. A. Evenson¹⁰, K. L. Fan²⁶, A. R. Fazely⁴⁶, N. Feigl⁴⁵, S. Fiedlschuster¹³, A. T. Fienberg¹², K. Filimonov¹⁹, C. Finley⁶, L. Fischer², D. Fox⁴², A. Franckowiak^{2,23}, E. Friedman²⁶, A. Fritz³⁰, P. Fürst²⁹, T. K. Gaisser¹⁰, J. Gallagher⁴⁷, E. Ganster²⁹, A. Garcia¹⁴, S. Garrappa², L. Gerhardt²⁸, A. Ghadimi⁴³, C. Glaser³¹, T. Glauch²⁴, T. Glüsenskamp¹³, J. G. Gonzalez¹⁰, S. Goswami⁴³, D. Grant³⁹, T. Grégoire¹², S. Griswold²⁵, C. Günther²⁹, P. Gutjahr⁷, C. Haack²⁴, A. Hallgren³¹, R. Halliday³⁹, L. Halve²⁹, F. Halzen¹⁵, M. Ha Minh²⁴, K. Hanson¹⁵, J. Hardin¹⁵, A. A. Harnisch³⁹, A. Haungs⁹, D. Hebecker⁴⁵, K. Helbing²², F. Henningsen²⁴, E. C. Hettinger³⁹, S. Hickford²², J. Hignight⁴⁸, C. Hill⁴⁹, G. C. Hill³⁴, K. D. Hoffman²⁶, R. Hoffmann²², B. Hokanson-Fasig¹⁵, K. Hoshina^{15,63}, F. Huang¹², M. Huber²⁴, T. Huber⁹, K. Hultqvist⁶, M. Hünnefeld⁷, R. Hussain¹⁵, K. Hymon⁷, S. In³⁸, N. Iovine⁴, A. Ishihara⁴⁹, M. Jansson⁶, G. S. Japaridze⁵⁰, M. Jeong³⁸, M. Jin¹⁴, B. J. P. Jones⁵¹, D. Kang⁹, W. Kang³⁸, X. Kang³⁶, A. Kappes³⁵, D. Kappesser³⁰, L. Kardum⁷, T. Karg², M. Karl²⁴, A. Karle¹⁵, U. Katz¹³, M. Kauer¹⁵, M. Kellermann²⁹, J. L. Kelley¹⁵, A. Kheirandish¹², K. Kin⁴⁹, T. Kintscher², J. Kiryluk³⁷, S. R. Klein^{19,28}, R. Koirala¹⁰, H. Kolanoski⁴⁵, T. Kontrimas²⁴, L. Köpke³⁰, C. Kopper³⁹, S. Kopper⁴³, D. J. Koskinen⁵, P. Koundal⁹, M. Kovacevich³⁶, M. Kowalski^{2,45}, T. Kozynets⁵, E. Kun²³, N. Kurahashi³⁶, N. Lad², C. Lagunas Gualda², J. L. Lanfranchi¹², M. J. Larson²⁶, F. Lauber²², J. P. Lazar^{14,15}, J. W. Lee³⁸, K. Leonard¹⁵, A. Leszczyńska³³, Y. Li¹², M. Lincetto²³, Q. R. Liu¹⁵, M. Liubarska⁴⁸, E. Lohfink³⁰, C. J. Lozano Mariscal³⁵, L. Lu¹⁵, F. Lucarelli⁸, A. Ludwig^{39,52}, W. Luszczak¹⁵, Y. Lyu^{19,28}, W. Y. Ma², J. Madsen¹⁵, K. B. M. Mahn³⁹, Y. Makino¹⁵, S. Mancina¹⁵, I. C. Mariş⁴, I. Martinez-Soler¹⁴, R. Maruyama⁵³, K. Mase⁴⁹, T. McElroy⁴⁸, F. McNally⁵⁴, J. V. Mead⁵, K. Meagher¹⁵, S. Mechal², A. Medina²¹, M. Meier⁴⁹, S. Meighen-Berger²⁴, J. Micallef³⁹, D. Mockler⁴, T. Montaruli⁸, R. W. Moore⁴⁸, R. Morse¹⁵, M. Moulai¹⁶, R. Naab², R. Nagai⁴⁹, U. Naumann²², J. Necker², L. V. Nguyễn³⁹, H. Niederhausen³⁹, M. U. Nisa³⁹, S. C. Nowicki³⁹, A. Obertacke Pollmann²², M. Oehler⁹, B. Oeyen⁵⁵, A. Olivás²⁶, E. O'Sullivan³¹, H. Pandya¹⁰, D. V. Pankova¹², N. Park⁴⁰, G. K. Parker⁵¹, E. N. Paudel¹⁰, L. Paul¹¹, C. Pérez de los Heros³¹, L. Peters²⁹, J. Peterson¹⁵, S. Philippen²⁹, S. Pieper²², M. Pittermann³³, A. Pizzuto¹⁵, M. Plum¹¹, Y. Popovych³⁰, A. Porcelli⁵⁵, M. Prado Rodriguez¹⁵, P. B. Price¹⁹, B. Pries³⁹, G. T. Przybylski²⁸, C. Raab⁴, A. Raissi³, M. Rameez⁵, K. Rawlins⁵⁶, I. C. Rea²⁴, A. Rehman¹⁰, P. Reichherzer²³, R. Reimann²⁹, G. Renzi⁴, E. Resconi²⁴, S. Reusch², W. Rhode⁷, M. Richman³⁶, B. Riedel¹⁵, E. J. Roberts³⁴, S. Robertson^{19,28}, G. Roellinghoff³⁸, M. Rongen³⁰, C. Rott^{38,57}, T. Ruhe⁷, D. Ryckbosch⁵⁵, D. Rysewyk Cantu³⁹, I. Safa^{14,15}, J. Saffer³³, S. E. Sanchez Herrera³⁹, A. Sandrock⁷, J. Sandroos³⁰, M. Santander⁴³, S. Sarkar⁵⁸, S. Sarkar⁴⁸, K. Satalecka², M. Schaufel²⁹, H. Schieler⁹, S. Schindler¹³, T. Schmidt²⁶, A. Schneider¹⁵, J. Schneider¹³, F. G. Schröder^{9,10}, L. Schumacher²⁴, G. Schwefer²⁹, S. Sclafani³⁶, D. Seckel¹⁰, S. Seunarine⁵⁹, A. Sharma³¹, S. Shefali³³, M. Silva¹⁵, B. Skrzypek¹⁴, B. Smithers⁵¹, R. Snihur¹⁵, J. Soedingrekso⁷, D. Soldin¹⁰, C. Spannfellner²⁴, G. M. Spiczak⁵⁹, C. Spiering², J. Stachurska², M. Stamatikos²¹, T. Stanev¹⁰, R. Stein², J. Stettner²⁹, A. Steuer³⁰, T. Stezelberger²⁸, T. Stürwald²², T. Stuttard⁵, G. W. Sullivan²⁶, I. Taboada³², S. Ter-Antonyan⁴⁶, S. Tilav¹⁰, F. Tischbein²⁹, K. Tollefson³⁹, C. Tönnis⁶⁰, S. Toscano⁴, D. Tosi¹⁵, A. Trettin², M. A. Tselengidou¹³, C. F. Tung³², A. Turcati²⁴, R. Turcotte⁹, C. F. Turley¹², J. P. Twagirayezu³⁹, B. Ty¹⁵, M. A. Unland Elorrieta³⁵, N. Valtonen-Mattila³¹, J. Vandenbroucke¹⁵, N. van Eijndhoven⁴¹, D. Vannerom¹⁶, J. van Santen², S. Verpoest⁵⁵, C. Walck⁶, T. B. Watson⁵¹, C. Weaver³⁹, P. Weigel¹⁶, A. Weindl⁹, M. J. Weiss¹², J. Weldert³⁰, C. Wendt¹⁵, J. Werthebach⁷, M. Weyrauch³³, N. Whitehorn^{39,52}, C. H. Wiebusch²⁹, D. R. Williams⁴³, M. Wolf²⁴, K. Woschnagg¹⁹, G. Wrede¹³, J. Wulff²³, X. W. Xu⁴⁶, J. P. Yanez⁴⁸, S. Yoshida⁴⁹, S. Yu³⁹, T. Yuan¹⁵, Z. Zhang³⁷, and P. Zhelnin¹⁴

IceCube Collaboration

¹ Department of Physics, Loyola University Chicago, Chicago, IL 60660, USA; analysis@icecube.wisc.edu² DESY, D-15738 Zeuthen, Germany³ Department of Physics and Astronomy, University of Canterbury, Private Bag 4800, Christchurch, New Zealand

- ⁴ Université Libre de Bruxelles, Science Faculty CP230, B-1050 Brussels, Belgium
⁵ Niels Bohr Institute, University of Copenhagen, DK-2100 Copenhagen, Denmark
⁶ Oskar Klein Centre and Department of Physics, Stockholm University, SE-10691 Stockholm, Sweden
⁷ Department of Physics, TU Dortmund University, D-44221 Dortmund, Germany
⁸ Département de physique nucléaire et corpusculaire, Université de Genève, CH-1211 Genève, Switzerland
⁹ Karlsruhe Institute of Technology, Institute for Astroparticle Physics, D-76021 Karlsruhe, Germany
¹⁰ Bartol Research Institute and Department of Physics and Astronomy, University of Delaware, Newark, DE 19716, USA
¹¹ Department of Physics, Marquette University, Milwaukee, WI, 53201, USA
¹² Department of Physics, Pennsylvania State University, University Park, PA 16802, USA
¹³ Erlangen Centre for Astroparticle Physics, Friedrich-Alexander-Universität Erlangen-Nürnberg, D-91058 Erlangen, Germany
¹⁴ Department of Physics and Laboratory for Particle Physics and Cosmology, Harvard University, Cambridge, MA 02138, USA
¹⁵ Department of Physics and Wisconsin IceCube Particle Astrophysics Center, University of Wisconsin—Madison, Madison, WI 53706, USA
¹⁶ Department of Physics, Massachusetts Institute of Technology, Cambridge, MA 02139, USA
¹⁷ Physics Department, South Dakota School of Mines and Technology, Rapid City, SD 57701, USA
¹⁸ Department of Physics and Astronomy, University of California, Irvine, CA 92697, USA
¹⁹ Department of Physics, University of California, Berkeley, CA 94720, USA
²⁰ Department of Astronomy, Ohio State University, Columbus, OH 43210, USA
²¹ Department of Physics and Center for Cosmology and Astro-Particle Physics, Ohio State University, Columbus, OH 43210, USA
²² Department of Physics, University of Wuppertal, D-42119 Wuppertal, Germany
²³ Fakultät für Physik & Astronomie, Ruhr-Universität Bochum, D-44780 Bochum, Germany
²⁴ Physik-department, Technische Universität München, D-85748 Garching, Germany
²⁵ Department of Physics and Astronomy, University of Rochester, Rochester, NY 14627, USA
²⁶ Department of Physics, University of Maryland, College Park, MD 20742, USA
²⁷ Department of Physics and Astronomy, University of Kansas, Lawrence, KS 66045, USA
²⁸ Lawrence Berkeley National Laboratory, Berkeley, CA 94720, USA
²⁹ III. Physikalisches Institut, RWTH Aachen University, D-52056 Aachen, Germany
³⁰ Institute of Physics, University of Mainz, Staudinger Weg 7, D-55099 Mainz, Germany
³¹ Department of Physics and Astronomy, Uppsala University, Box 516, S-75120 Uppsala, Sweden
³² School of Physics and Center for Relativistic Astrophysics, Georgia Institute of Technology, Atlanta, GA 30332, USA
³³ Karlsruhe Institute of Technology, Institute of Experimental Particle Physics, D-76021 Karlsruhe, Germany
³⁴ Department of Physics, University of Adelaide, Adelaide, 5005, Australia
³⁵ Institut für Kernphysik, Westfälische Wilhelms-Universität Münster, D-48149 Münster, Germany
³⁶ Department of Physics, Drexel University, 3141 Chestnut Street, Philadelphia, PA 19104, USA
³⁷ Department of Physics and Astronomy, Stony Brook University, Stony Brook, NY 11794-3800, USA
³⁸ Department of Physics, Sungkyunkwan University, Suwon 16419, Republic of Korea
³⁹ Department of Physics and Astronomy, Michigan State University, East Lansing, MI 48824, USA
⁴⁰ Department of Physics, Engineering Physics, and Astronomy, Queen's University, Kingston, ON K7L 3N6, Canada
⁴¹ Vrije Universiteit Brussel (VUB), Dienst ELEM, B-1050 Brussels, Belgium
⁴² Department of Astronomy and Astrophysics, Pennsylvania State University, University Park, PA 16802, USA
⁴³ Department of Physics and Astronomy, University of Alabama, Tuscaloosa, AL 35487, USA
⁴⁴ Centre for Cosmology, Particle Physics and Phenomenology—CP3, Université catholique de Louvain, Louvain-la-Neuve, Belgium
⁴⁵ Institut für Physik, Humboldt-Universität zu Berlin, D-12489 Berlin, Germany
⁴⁶ Department of Physics, Southern University, Baton Rouge, LA 70813, USA
⁴⁷ Department of Astronomy, University of Wisconsin—Madison, Madison, WI 53706, USA
⁴⁸ Department of Physics, University of Alberta, Edmonton, Alberta, T6G 2E1, Canada
⁴⁹ Department of Physics and Institute for Global Prominent Research, Chiba University, Chiba 263-8522, Japan
⁵⁰ CTSPS, Clark-Atlanta University, Atlanta, GA 30314, USA
⁵¹ Department of Physics, University of Texas at Arlington, 502 Yates Street, Science Hall, Rm. 108, Box 19059, Arlington, TX 76019, USA
⁵² Department of Physics and Astronomy, UCLA, Los Angeles, CA 90095, USA
⁵³ Department of Physics, Yale University, New Haven, CT 06520, USA
⁵⁴ Department of Physics, Mercer University, Macon, GA 31207-0001, USA
⁵⁵ Department of Physics and Astronomy, University of Gent, B-9000 Gent, Belgium
⁵⁶ Department of Physics and Astronomy, University of Alaska Anchorage, 3211 Providence Drive, Anchorage, AK 99508, USA
⁵⁷ Department of Physics and Astronomy, University of Utah, Salt Lake City, UT 84112, USA
⁵⁸ Department of Physics, University of Oxford, Parks Road, Oxford OX1 3PU, UK
⁵⁹ Department of Physics, University of Wisconsin, River Falls, WI 54022, USA
⁶⁰ Institute of Basic Science, Sungkyunkwan University, Suwon 16419, Republic of Korea

Received 2021 November 19; revised 2022 January 14; accepted 2022 January 18; published 2022 March 25

Abstract

We present a measurement of the high-energy astrophysical muon–neutrino flux with the IceCube Neutrino Observatory. The measurement uses a high-purity selection of 650k neutrino-induced muon tracks from the

⁶¹ also at Università di Padova, I-35131 Padova, Italy

⁶² also at National Research Nuclear University, Moscow Engineering Physics Institute (MEPhI), Moscow 115409, Russia

⁶³ also at Earthquake Research Institute, University of Tokyo, Bunkyo, Tokyo 113-0032, Japan



Original content from this work may be used under the terms of the [Creative Commons Attribution 4.0 licence](https://creativecommons.org/licenses/by/4.0/). Any further distribution of this work must maintain attribution to the author(s) and the title of the work, journal citation and DOI.

northern celestial hemisphere, corresponding to 9.5 yr of experimental data. With respect to previous publications, the measurement is improved by the increased size of the event sample and the extended model testing beyond simple power-law hypotheses. An updated treatment of systematic uncertainties and atmospheric background fluxes has been implemented based on recent models. The best-fit single power-law parameterization for the astrophysical energy spectrum results in a normalization of $\phi_{@100\text{TeV}}^{\nu_i+\bar{\nu}_i} = 1.44_{-0.26}^{+0.25} \times 10^{-18} \text{ GeV}^{-1}\text{cm}^{-2}\text{s}^{-1}\text{sr}^{-1}$ and a spectral index $\gamma_{\text{SPL}} = 2.37_{-0.09}^{+0.09}$, constrained in the energy range from 15 TeV to 5 PeV. The model tests include a single power law with a spectral cutoff at high energies, a log-parabola model, several source-class-specific flux predictions from the literature, and a model-independent spectral unfolding. The data are consistent with a single power-law hypothesis, however, spectra with softening above one PeV are statistically more favorable at a two-sigma level.

Unified Astronomy Thesaurus concepts: [Neutrino astronomy \(1100\)](#); [High energy astrophysics \(739\)](#)

1. Introduction

The field of neutrino astronomy has gained momentum since the IceCube collaboration discovered a diffuse flux of astrophysical neutrinos in multiple detection channels (Aartsen et al. 2013, 2016, 2020c). Prominent examples of this continuous journey are the identification of a first joint source of high-energy gamma rays and neutrinos, TXS 0506 + 056 (Aartsen et al. 2018a, 2018b), increasing hints for the emission of high-energy neutrinos from the radio galaxy NGC1068 (Aartsen et al. 2020a), and detection of a particle shower at the Glashow resonance energy (Aartsen et al. 2021a).

Measuring the total observed flux strength and energy spectrum of high-energy astrophysical neutrinos complements direct searches for neutrino sources and is important to understand the processes behind the acceleration and propagation of high-energy cosmic rays.

The origin of high-energy neutrinos has been predicted from nonthermal Galactic and extragalactic sources, as reviewed in Learned & Mannheim (2000), Becker (2008), Halzen & Klein (2010), and Ahlers & Halzen (2018). As the diffuse flux detected by IceCube is close to isotropically distributed and does not follow the Galactic plane, Galactic sources have been disfavored, while still being discussed as a subdominant contribution; see Becker Tjus & Merten (2020) for a summary. The prompt phase of gamma-ray bursts (GRBs) has also been excluded as a dominant neutrino source by dedicated IceCube analyses (Abbasi et al. 2012a; Aartsen et al. 2017d).

However, prominent possible sources of neutrinos exist; for example, choked GRBs in dense environments (Senno et al. 2016; Biehl et al. 2018). A second promising source of high-energetic extragalactic sources is active galactic nuclei (AGNs; Murase et al. 2014; Kimura et al. 2015; Liu et al. 2018), including BL Lac objects (Tavecchio & Ghisellini 2015; Padovani et al. 2015). Tidal disruption events (TDEs) are a third promising source class of high-energy neutrinos and ultra-high-energy cosmic rays (Farrar & Piran 2014; Dai & Fang 2017; Guépin & Kotera 2017; Lunardini & Winter 2017; Senno et al. 2017; Biehl et al. 2018; Stein et al. 2021). Here, particle acceleration could be driven by either a hidden jet, a hidden subrelativistic wind, emission from a hot corona above the accretion disk, or radiatively inefficient accretion flows (see Hayasaki 2021 for a review). Starburst galaxies have also been considered a possibly contributing source class (Loeb & Waxman 2006; Tamborra et al. 2014). These models have in common that they expect neutrinos to be produced when a power-law-distributed population of cosmic rays interacts with gas or photon fields in the source or its vicinity in order to produce pions and kaons, which in turn, decay into neutrinos. These neutrinos would follow the same power law as the initial cosmic-ray population, however, effects like an energy-dependent

cross section, breaks, or spectral features in the accelerated cosmic-ray spectrum can lead to deviations from a pure power law. In this paper, we present an improved measurement of the energy spectrum of astrophysical muon neutrinos, including models beyond the single power law and tests of a selection of the abovementioned models. Also, we update the sample of up-going muon tracks ($\theta_{\text{zenith}} > 85^\circ$) originating from the northern celestial hemisphere (Aartsen et al. 2016).

2. Data Sample

The IceCube Neutrino Observatory is a gigaton-scale Cherenkov detector embedded in the Antarctic ice at the geographical South Pole (Aartsen et al. 2017a). Its fundamental building blocks are 5160 digital optical modules (DOMs). These spherical detection units each include a 10" (25.4 cm) photomultiplier tube suited to detect weak light signals (Abbasi et al. 2010), read-out, and digitization electronics (Abbasi et al. 2009), and are positioned on 86 vertical cable strings that are arranged in a hexagonal grid. In this analysis, the data from eight strings forming the denser instrumented region of the DeepCore array (Abbasi et al. 2012b) are excluded in favor of a more homogeneous detector geometry. Neutrinos are detected indirectly via the Cherenkov light emitted by charged relativistic secondary particles. These emerge from deep inelastic neutrino–nucleon interactions which occur in the instrument and the surrounding ice or the bedrock below IceCube. The final detector configuration (IC86) was completed in 2010 December. Recording of data already occurred prior to finalization with partial configurations. Data from two such partial configurations, IC59 and IC79, are included in this analysis, with the number indicating the number of active strings.

The presented study is based on a sample of through-going and starting muon tracks detected between 2009 May 20 and 2018 December 31. Muons can travel through the ice for hundreds or thousands of meters, producing track-like signatures in the detector. The event selection is identical to the one presented in Aartsen et al. (2016). It focuses on events with extended track-like signatures and filters out cascade-like events, which are events where the light emission region is small compared to the detector string spacing of 125 m. Such events can, for example, arise from neutral current interactions or electron–neutrino-induced charged current interactions. Neutrino-induced muon tracks are dominated by charged current interactions of muon neutrinos. A small additional energy-dependent contribution arises from muonic tau decays in tau neutrino interactions which contributes roughly 5% (Stettner 2021). This is included in the signal expectation of the analysis. The contribution of tracks from Glashow resonance interactions (Aartsen et al. 2021a) is negligible in this analysis. By restricting the field of view of the detector to zenith angles

Table 1
Summary of the Event Sample

Data-taking Season	Zenith Range (deg)	Effective Livetime ^a (years)	Number of Events	Pass-2
IC59	90 – 180	0.9538	21411	No
IC79—IC86-2018	85 – 180	8.181	651377	Yes
Total		9.135	672788	

Notes. See text for a description of the Pass-2 re-calibration campaign that was conducted for all data after 2010 May.

^a The livetime for the season IC79 has been corrected by a factor 0.94 to account for the lower expected trigger rate of the partial detector configuration.

$\theta_{\text{zenith}} > 85^\circ$, the overwhelming background of atmospheric muons from cosmic-ray-induced air showers is successfully suppressed (purity $> 99.8\%$) as these muons are stopped in the Earth or the ice overburden before reaching IceCube. The direction of the selected muon-track events is obtained using the MPE algorithm with tabulated ice properties (Ahrens et al. 2004; Schatto 2014) and the muon energy is reconstructed using the truncated energy (DOM’s method) algorithm described in Abbasi et al. (2013) which takes the stochastic energy losses of high-energy muons into account, resulting in an energy resolution of 0.22 in $\log_{10} E_\mu$ (Abbasi et al. 2013). The resulting proxy energy $E_{\mu,\text{proxy}}$ is inherently only a lower limit on the true muon and primary neutrino energies, as the neutrino–nucleon interactions can occur outside the detection volume.

Compared to the previous iteration of this analysis based on six years of data, more than 300,000 new events were detected and analyzed; see Table 1. In addition, the full sample of events was reprocessed within the scope of IceCube’s Pass-2 campaign (Aartsen et al. 2020b) to apply the latest detector calibrations to archival data as well. In this campaign, the same event filtering, selections, and reconstructions are consistently applied to all data after 2010 May (IC79–IC86-2018), while IC59 is still treated separately in the analysis. More details can be found in Stettner (2021).

Five new events with reconstructed energies $E_{\mu,\text{proxy}} \gtrsim 200$ TeV are observed in the additional data-taking period. This energy approximately corresponds to a zenith-averaged signalness $S \gtrsim 0.5$:

$$S(E_\mu) = \frac{\Phi_{\text{signal}}(E_\mu)}{\Phi_{\text{signal}}(E_\mu) + \Phi_{\text{background}}(E_\mu)} \gtrsim 0.5. \quad (1)$$

So, for these events, the probability of the particle belonging to the differential astrophysical signal flux Φ_{signal} exceeds 0.5.

The event with the highest reconstructed energy from this additional period is the horizontal track event with ID II.32 (Table 7) which has an energy of more than $E_{\mu,\text{proxy}} \gtrsim 1.1$ PeV, and has also been reported as a real-time alert (Aartsen et al. 2017b). The event with the overall highest reconstructed energy has the table ID II.22, and is described in detail in Aartsen et al. (2016). The threshold $E_{\mu,\text{proxy}} \gtrsim 200$ TeV to report individual events does not change significantly with the updated best-fit parameterization for the energy spectrum discussed in Section 4.⁶⁴ The modified calibrations, however, which include a -4% shift of the charge corresponding to a single photoelectron, do lead to changes of the reconstructed energies and directions of some of the events that have been reported in Aartsen et al. (2016), shown in the rightmost three columns of Table 7. The impact on the reported quantities is

⁶⁴ With the updated spectral distribution as reported in this paper, a more precise threshold would correspond to an energy proxy of 185 TeV. For consistency with previously reported events, we keep the original threshold definition.

small, especially for the directional reconstructions (most directions change by less than 0.1° and stay well within their uncertainty ranges), but for single events with special topology, deviations in reconstructed energy can occur. Notably, such deviations arise for data taken in 2010 (IC79), where the information from the DeepCore strings is now excluded. As a consequence, six of the previously reported events fall below the threshold of $E_{\mu,\text{proxy}} \gtrsim 200$ TeV. Additionally, one event (ID6 in Aartsen et al. 2016, IC79-season) does not pass the event selection anymore, because the IC79 season data as used in Aartsen et al. (2016) were based on an individual dedicated event selection, which has now been unified with the treatment of later seasons where the event selection includes additional measures to reject cascade-like events more efficiently. These had not been applied to the IC79 data previously. For a detailed list of all events and the respective changes, see Table 7 in the supplementary material.

In order to calculate the expected number of events at the detector, a large sample of events is simulated, taking into account the following propagation steps: the propagation of neutrinos through matter, primary neutrino–nucleon interactions (CSMS cross section: Cooper-Sarkar et al. 2011), propagation of secondary particles through the ice (PROPOSAL code: Köhne et al. 2013), and the production and propagation of Cherenkov photons in the detector medium (Chirkin 2015), CLSim code: Chirkin et al. (2019). They are modeled in detail before the final detector electronics and data acquisition are simulated. In addition, these simulations are repeated with altered assumptions on systematic uncertainties, e.g., scattering or absorption of the Cherenkov photons in the natural glacier and in the man-made boreholes.

3. Analysis Method

The measurement of the energy spectrum of astrophysical muon neutrinos is performed via a forward-folding fit: the experimentally observed events are compared to the simulation-based expectation in a two-dimensional histogram as a function of reconstructed zenith angle and reconstructed muon energy. By maximizing the Poisson likelihood from Equation (2), the best-fitting flux hypothesis is obtained for the observed data D , which consist of a number n of observed events per bin:

$$\mathcal{L}(D|\vec{\theta}, \vec{\xi}) = \prod_{\text{bin}}^{N_{\text{bins}}} p_{\text{Poisson}}(n_{\text{bin}}, \mu_{\text{bin}}(\vec{\theta}, \vec{\xi})). \quad (2)$$

The expected number of events at the detector, μ , is modeled as a function of signal parameters $\vec{\theta}$ and nuisance parameters $\vec{\xi}$. The latter absorb systematic uncertainties of the measurement; see Section 3.1.

The two-dimensional analysis histogram consists of 50 energy bins equally spaced in $10^2 < \log_{10}(E_{\mu,\text{proxy}}/\text{GeV}) < 10^7$

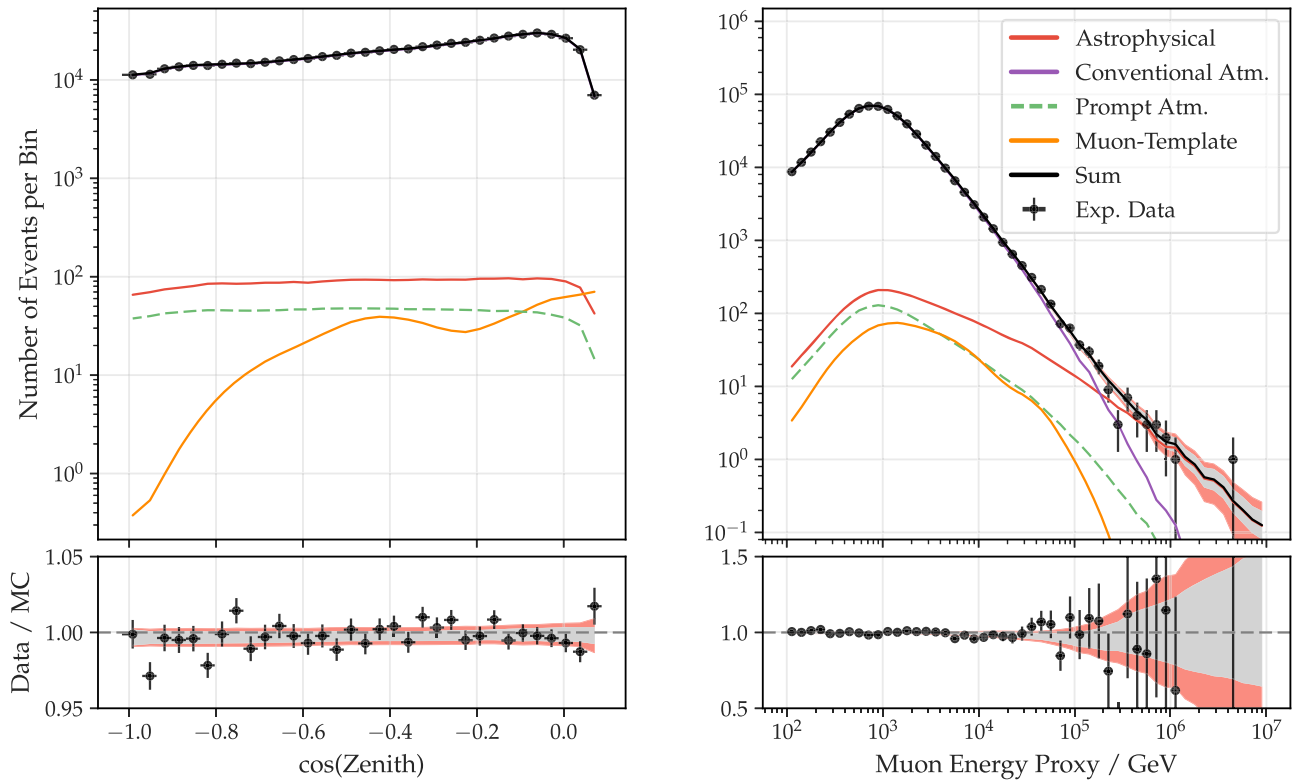


Figure 1. Single power-law model: best-fit distributions and one-dimensional projection on reconstructed zenith angle and muon energy. The experimental data (black dots) are shown together with the best-fit expectation from simulations. Data taken in the IC59 detector configuration are kept in a separate analysis histogram. The conventional atmospheric component (purple) dominates the total flux for all zenith angles. Except for the highest energies, the line is thus hidden below the overall sum (black). The astrophysical component (red) is modeled as a single power law. The prompt component is drawn at nominal prediction for visualization (green-dashed) although a zero best-fit normalization is obtained. The best-fit expectation for the remaining background of muons is shown by the orange line. The central 68% range of the best-fit expectation is drawn as a gray band. It is obtained by varying all fit parameters according to their joint posterior distribution. The orange band additionally shows the statistical uncertainty of the simulated data.

and 33 bins spaced in reconstructed $\cos(\text{Zenith})$ ranging from 85° to 180° . The binning is identical to the one used in Aartsen et al. (2016) with $N_{\text{bins}} = 1650$.

Four flux components are considered and the expected number of events is given as a sum of these components per bin. First and second, atmospheric backgrounds are considered: conventional atmospheric neutrinos, emerging from the decay of pions and kaons in cosmic-ray-induced air showers and prompt atmospheric neutrinos from the decay of heavy charmed hadrons in the same showers. For both contributions, the prediction is updated with respect to Aartsen et al. (2016), which used a prediction from Honda et al. (2007). The software Matrix Cascade Equation solver, MCEq (Fedynitch et al. 2015), is employed assuming the flux model Gaisser-H4a (Gaisser 2012) for primary cosmic rays and the hadronic interaction model Sibyll 2.3c (Fedynitch et al. 2019). Third, a subdominant contamination from atmospheric muons is expected and modeled based on a large sample of cosmic-ray air showers. The resulting model for this background flux is denoted as the muon template. It is simulated with the CORSIKA package (Heck et al. 1998), assuming the mentioned primary cosmic-ray and hadronic interaction models. Fourth, and most important, a signal component of astrophysical neutrinos is considered. It represents the cumulative flux from all sources of high-energy astrophysical neutrinos, which we assume to be isotropic.

A wide range of parameterizations for the energy spectrum of the astrophysical component are investigated in Sections 4 and 5. The expected rate of events as a function of zenith and

energy is visualized in Figure 1 for all four components assuming a single power-law spectrum of astrophysical neutrinos. Figure 2 further illustrates the potential to measure astrophysical neutrinos at high energies by showing the expected ratio of astrophysical signal over background.

3.1. Updated Treatment of Systematic Uncertainties

In order to absorb systematic uncertainties of the measurement, nuisance parameters are introduced in the fit. The first class of systematic uncertainties covers the detector response and reconstruction quality of IceCube. Optical properties of the natural ice and the ice in the man-made boreholes are considered as well as the optical detection efficiency. Compared to the last iteration of this analysis, the model of optical properties in the natural ice has been updated (Spice 3.2.1: Rongen 2019) and the impact of the ice in the boreholes (unified hole-ice model: Eller 2019) is now taken into account as an additional source of uncertainty. For each of these systematic uncertainties, dedicated simulations have been performed and the impact on reconstructed energy and zenith have been parameterized.

The second class of systematic uncertainties arises from the flux predictions of atmospheric neutrinos. Since the absolute normalization of the primary cosmic-ray flux and the yield of neutrinos from cosmic-ray-induced air showers are not known precisely, the absolute flux normalizations ϕ_{conv} and ϕ_{prompt} are free fit parameters. Additionally, the parameters $\Delta\gamma_{\text{CR}}$ (CR spectral index shift) and $\lambda_{\text{CR Model}}$, which is a prior-constrained linear interpolation between the Gaisser-H4a and GST-4gen

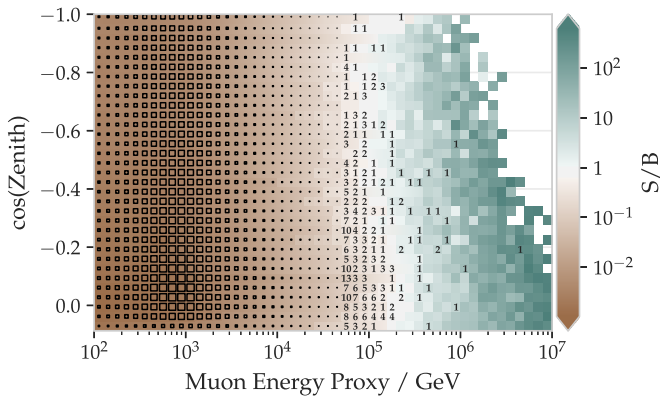


Figure 2. The color indicates the ratio of the signal (astrophysical) over the background (atmospheric and muonic) component expectation assuming the best-fit energy spectrum obtained in Section 4. The binning is equivalent to the two-dimensional histogram used in the analysis. For energies above $E_{\mu, \text{proxy}} \gtrsim 50$ TeV, the number of observed events per bin is indicated, in the bins below this threshold; the number of events is proportional to the size of the black squares, with the maximum number of data events in a single bin being 3204.

Table 2

Single Power-law Model: Best-fit Parameters Assuming a Single Power-law Energy Spectrum

Astrophysical Norm. $\phi_{\text{astro}}/C_{\text{units}}$	$1.44^{+0.25}_{-0.26}$
Spectral Index γ_{SPL}	$2.37^{+0.09}_{-0.09}$

Note. The astrophysical normalization is given in units of $C_{\text{units}} = 10^{-18} \text{ GeV}^{-1} \text{ cm}^{-2} \text{ s}^{-1} \text{ sr}^{-1}$. Confidence intervals (68%) are constructed from one-dimensional profile likelihood scans employing Wilks' theorem (Wilks 1938).

flux models (Gaisser 2012; Gaisser et al. 2013), are introduced analogously to Aartsen et al. (2016) in order to cover uncertainties on the exact spectral shape of the primary cosmic-ray flux. This shape affects all atmospheric flux components alike. Furthermore, we update the treatment of atmospheric flux uncertainties by adopting the scheme from Barr et al. (2006). By varying the relevant parameters H (pions), W (kaons), Y (kaons), and Z (kaons) within their estimated prior ranges and repeating the calculation of atmospheric fluxes, uncertainties from hadronic interaction models are covered by this suite of parameters. The parameters affecting the spectral shapes of the atmospheric fluxes are correlated with the absolute normalizations. For more details, see A.1 and Figure 6 in the supplementary material. Finally, the absolute normalization of the subdominant muon contamination is included as a parameter and allowed to vary within its estimated prior range as well, which is a Gaussian with a width of 0.5.

4. Results: Single Power-law Model

The result of the likelihood fit is shown as a one-dimensional projection by the solid black line in Figure 1 together with the experimental data. At energies above $E_{\mu, \text{proxy}} \gtrsim 100$ TeV, the excess of astrophysical neutrinos above the atmospheric components is clearly visible. Overall, the data are well described by the sum of atmospheric components and an astrophysical component following the standard paradigm of a single power-law energy spectrum. Figure 7 in the supplementary material shows the

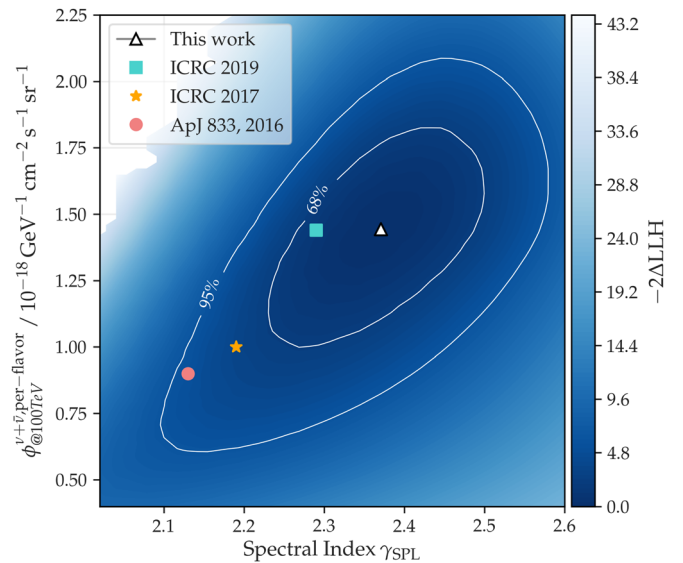


Figure 3. Single power-law model: profile likelihood landscape as a function of spectral index and astrophysical normalization. The best-fit parameters are marked as a white triangle. The turquoise square (Stettner & IceCube Collaboration 2019, $\gamma = 2.28^{+0.08}_{-0.09}$, $\Phi = 1.44^{+0.25}_{-0.24}$), the orange star (Haack & IceCube Collaboration, 2018, $\gamma = 2.19^{+0.10}_{-0.10}$, $\Phi = 1.01^{+0.26}_{-0.23}$), and the pink circle (Aartsen et al. 2016, $\gamma = 2.13^{+0.13}_{-0.13}$, $\Phi = 0.90^{+0.30}_{-0.27}$) mark results of previous measurements.

statistical pull for all bins in the two-dimensional histogram indicating no obvious mismatches. Taking the systematic and statistical uncertainty of the best-fit expectation into account, a $\chi^2/(\text{degrees of freedom})$ for the single power-law fit is calculated to be 1.0, resulting in a p -value of 50% and confirming that the fit result is a viable description of the measured data. The corresponding best-fit parameters of the astrophysical flux are listed in Table 2 and the profiled likelihood landscape of the two astrophysical signal parameters is shown in Figure 3. The sensitive energy range of the astrophysical measurement is determined by comparing the per-bin likelihood values of the best-fit hypothesis to the values obtained when repeating the fit assuming a background hypothesis. The true neutrino energy distribution is then weighted with these likelihood differences, and the central 90% range of the obtained distribution is $E_\nu = 15 \text{ TeV} - 5 \text{ PeV}$. This energy range extends to lower energies than previous measurements, where this energy range extended from $E_\nu = 200 \text{ TeV} - 8 \text{ PeV}$ (Aartsen et al. 2016). This change is driven by the updated modeling of the conventional atmospheric flux in this energy region.

Compared to the previous analysis by Aartsen et al. (2016), a slightly softer spectral index of $\gamma_{\text{SPL}} = 2.37^{+0.09}_{-0.09}$ is obtained. Figure 3 shows the best-fit points of the previous measurements, and the updates and changes between them are listed here as an overview. The measurements from Aartsen et al. (2016) and Haack & IceCube Collaboration (2018) are based on the same event selection and analysis method, with two years of additional data included in the latter. The changes between Haack & IceCube Collaboration (2018) and the results from Stettner & IceCube Collaboration (2019) are mostly driven by the updated atmospheric background prediction. Additionally, the Barr parameters are introduced, resulting in more fit freedom at medium energies, and the subdominant effects of neutrino oscillations are considered. The updates to the detector simulations (Pass-2) also occurred in between these analyses, but have a negligible effect on the fit result and

uncertainty. Changes between the result reported in Stettner & IceCube Collaboration (2019) and this analysis are a new event simulation including the effects of the hole-ice (Eller 2019) and the addition of the subdominant muon component. A purely atmospheric hypothesis can be excluded with very high significance at a 5.6σ level. Note that this significance is smaller than previously reported results because of the updated, more conservative treatment of systematic uncertainties as well as the observed softening of the spectral index.

4.1. Prompt Atmospheric Neutrinos

We find that the normalization of prompt atmospheric neutrinos is constrained less strongly compared to the last publication. This is related to the observed softening of the spectral index of the astrophysical neutrino flux, resulting in an overall more similar shape of the two flux components. For the calculation of a prompt limit, the dominating astrophysical flux in the regions below the sensitive energy range of this analysis poses a fundamental limitation to our ability to quantitatively constrain the subdominant flux of prompt neutrinos.

The best fit of the prompt normalization is still zero, independent of the different assumed astrophysical flux parameterizations discussed in Section 5. The prompt flux model prediction from MCEq (Sibyll 2.3c; H4a) is used here compared to the ERS prediction (Enberg et al. 2008) in the last publication (Aartsen et al. 2016), these two models predict very similar fluxes. A more recent model (Bhattacharya et al. 2015) predicts a prompt atmospheric flux component with about a factor of three smaller normalization.

It has been checked in detail that the measurement of the astrophysical component is not impacted by the prompt flux normalization: for example, we find a spectral index of $\gamma_{\text{SPL}} = 2.33$, well within the quoted uncertainty range, if the likelihood fit is repeated with the prompt component fixed to its nominal prediction ($\phi_{\text{prompt}} = 1.0$). Also, the observed suppression of the prompt component occurs at similar strength when the likelihood fit is repeated while excluding energies above ≈ 15 TeV, confining it to an energy region dominated by conventional atmospheric neutrinos and well below the sensitive energy range for astrophysical neutrinos. The exact reason for this nonobservation remains an open question and an updated limit on the prompt flux normalization with respect to Aartsen et al. (2016) is not computed here.

5. Results: Beyond the Single Power Law

Power-law energy spectra are well motivated from the assumed acceleration mechanisms of cosmic rays, but they extrapolate over large energy ranges and potential structures in the energy spectrum can thus not be identified. In this section, a number of parameterizations beyond a single power law are compared to the experimental data. Parameterizations with more than three signal parameters are, however, not considered because the statistics of observed events with high signalness is too low to constrain more fit parameters.

5.1. Power Law with Cutoff

The first natural extension to the single power law would be a cutoff in the energy spectrum, e.g., introduced if an astrophysical source of cosmic rays (and neutrinos) reaches its maximum energy. The flux parameterization given in Equation (3) extends

Table 3
Single Power Law with Cutoff: Best-fit Parameters

Astrophysical Norm. $\phi_{\text{cutoff}}/C_{\text{units}}$	$1.64^{+0.39}_{-0.36}$
Spectral Index γ_{cutoff}	$2.0^{+0.22}_{-0.28}$
Cutoff Energy $E_{\text{cutoff}}/\text{PeV}$	$1.25^{+1.72}_{-0.56}$
Significance over SPL	$2\Delta\text{LLH} = 4.24$ $p(> 2\Delta\text{LLH} \text{SPL}) = 6.1\%$

Note. Confidence intervals (68%) are constructed from one-dimensional profile likelihood scans employing Wilks' theorem.

Table 4
Log-parabola Model: Best-fit Parameters

Log-parabola Norm. $\phi_{\text{LogParab.}}/C_{\text{units}}$	$1.79^{+0.40}_{-0.38}$
Spectral Index $\alpha_{\text{LogParab.}}$	$2.03^{+0.22}_{-0.31}$
Curvature parameter $\beta_{\text{LogParab.}}$	$0.45^{+0.29}_{-0.22}$
Significance over SPL	$2\Delta\text{LLH} = 6.82$ $p(> 2\Delta\text{LLH} \text{SPL}) = 1.3\%$

Note. Confidence intervals (68%) are constructed from one-dimensional profile likelihood scans employing Wilks' theorem.

the single power law with an exponentially decaying term. The cutoff neutrino energy E_{cutoff} is consequently added as a third signal parameter in the likelihood fit:

$$\Phi_{\text{astro.}}^{\nu_{\mu}+\bar{\nu}_{\mu}}(E_{\nu}) = \phi_{\text{cutoff}} \times \left(\frac{E_{\nu}}{100 \text{ TeV}} \right)^{-\gamma_{\text{cutoff}}} \times e^{\left(\frac{-E_{\nu}}{E_{\text{cutoff}}} \right)}. \quad (3)$$

Table 3 lists the obtained fit result using this parameterization: while the astrophysical normalization does not change strongly, a hard spectral index of $\gamma_{\text{cutoff}} = 2.0^{+0.22}_{-0.28}$ and a cutoff energy of $E_{\text{cutoff}} = 1.25^{+1.72}_{-0.56}$ PeV is found. Compared to the single power-law hypothesis, the fit improves by $2\Delta\text{LLH} = 4.24$. The probability to randomly achieve any such improvement by introducing E_{cutoff} corresponds to a p -value of $p(> 2\Delta\text{LLH}|\text{SPL}) = 6.1\%$, which is calculated from pseudo-experiments obtained from Monte Carlo simulations.

5.2. Log-parabola Model

Similarly to the cutoff hypothesis, the log-parabola model, widely used in gamma-ray astronomy, extends the single power law and allows for curvature of the spectrum. Its parameterization is given in Equation (4) and Table 4 lists the obtained best-fit parameters of the likelihood fit with an astrophysical component following this model. Again, a hard spectral index of $\alpha_{\text{LogParab.}} = 2.03^{+0.22}_{-0.31}$ is obtained, and the best fit of the curvature parameter is $\beta_{\text{LogParab.}} = 0.45^{+0.29}_{-0.22}$. Compared to the single power-law hypothesis, which corresponds to $\beta_{\text{LogParab.}} = 0$, the description of the experimental data is improved by $2\Delta\text{LLH} = 6.82$. Analogously to the treatment for the cutoff hypothesis, this can be translated to a p -value of $p(> 2\Delta\text{LLH}|\text{SPL}) = 1.3\%$.

$$\Phi_{\text{astro.}}^{\nu_{\mu}+\bar{\nu}_{\mu}}(E_{\nu}) = \phi_{\text{LogParab.}} \times \left(\frac{E_{\nu}}{100 \text{ TeV}} \right)^{-\alpha_{\text{LogParab.}} - \beta_{\text{LogParab.}} \log\left(\frac{E_{\nu}}{100 \text{ TeV}}\right)} \quad (4)$$

Table 5

Piece-wise Parameterization: Energy Ranges and Result of the Likelihood Fit

	Energy Range (E_ν)	Norm. ($\phi_{\text{piece}}^i / C_{\text{units}}$)
Piece 1 ^a	100 GeV–15 TeV	$0.0^{+3.1}$
Piece 2	15 TeV–104 TeV	$2.22^{+0.8}_{-0.8}$
Piece 3	104 TeV–721 TeV	$1.21^{+0.32}_{-0.31}$
Piece 4	721 TeV–5 PeV	$0.33^{+0.22}_{-0.18}$
Piece 5 ^a	5 PeV–100 PeV	$0.0^{+0.41}$

Note. Note that all piece-wise normalizations are optimized simultaneously in the fit, i.e., correlations between the segments are fully taken into account. The given 68.27% uncertainty ranges are obtained from one-dimensional profile likelihood scans. ^aPieces 1 and 5 have been added to cover the full energy range here; upper limits (90% CL) are computed.

5.3. Piece-wise Parameterization

In order to overcome the limitations of the parameterizations discussed in previous sections, a “piece-wise” model is introduced. Here, the energy spectrum is described as sum of power laws with a fixed spectral index ($\gamma = 2.0$) in pre-defined, fixed segments of neutrino energy. This allows for measuring the flux strength in a well-defined range of neutrino energy and enables easy comparison to predictions from the literature and to other measurements. The total flux strength is then given by Equation (5), where the flux normalizations per bin ϕ_{piece}^i are fit parameters and E_{low}^i and E_{high}^i form the bounds of bin i .

$$\Phi_{\text{astro.}}^{\nu_\mu + \bar{\nu}_\mu}(E_\nu) = \sum_i^{\text{pieces}} \chi(E_\nu) \cdot \phi_{\text{piece}}^i \cdot \left(\frac{E_\nu}{100 \text{ TeV}}\right)^{-2.0}$$

$$\chi(E_\nu) = \begin{cases} 1 & \text{if } E_{\text{low}}^i < E_\nu < E_{\text{high}}^i \\ 0 & \text{else} \end{cases} \quad (5)$$

Prior to performing the fit on the experimental data, the energy ranges of the segments were defined to be equally spaced in log-energy spanning the sensitive energy range of the astrophysical measurement (see Section 4) with three segments. Additionally, one segment above and below have been added, respectively, to cover the full energy range. The full parameterization of the astrophysical flux is given in Equation (5), and the energy ranges and obtained best-fit normalizations ϕ_{piece}^i are listed in Table 5. Figure 4 visualizes the obtained flux measurement of the piece-wise parameterization together with the results of the single power law, power law with cutoff, and log-parabola models. In all models beyond the single power law, hints for a softening of the spectral shape as a function of energy are found.

5.4. Flux Predictions for Specific Source Classes

Besides the wide range of generic parameterizations for the energy spectrum discussed in the sections above, it is also possible to compare the experimental data to source-class specific flux predictions directly. The total astrophysical flux may originate from multiple source classes, thus it is not expected that a single flux prediction can fully explain the observed data. Instead, we model the total astrophysical component as sum of the predicted energy spectrum model times a free normalization ϕ_{model} and a single power law to cover other potential flux contributions:

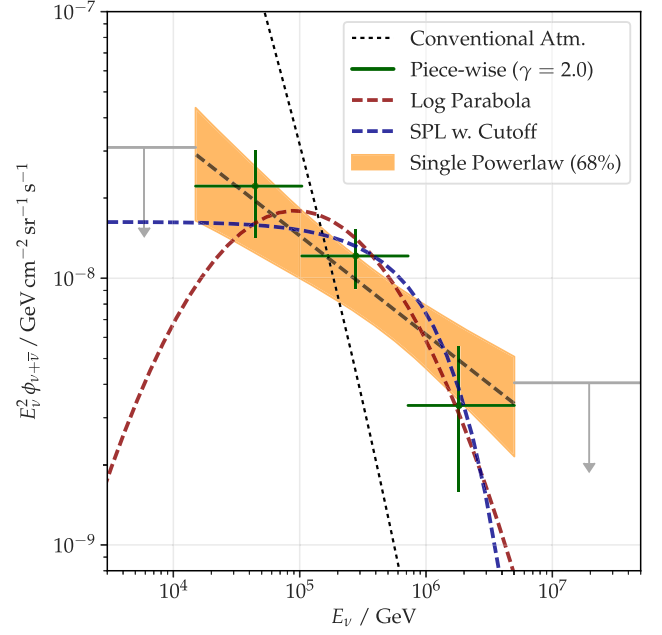


Figure 4. Summary of best-fit models for the astrophysical neutrino flux. The bins from the piece-wise unfolding are marked in green and in gray wherever only upper limits are calculated. The single power-law band is drawn in the sensitive energy range as defined in Section 4. All models with more degrees of freedom than the single power law show a trend from a hard spectral shape at medium energies to a softer spectrum at highest energies.

$$\Phi_{\text{astro.}}^{\nu_\mu + \bar{\nu}_\mu}(E_\nu) = \phi_{\text{model}} \times \text{Model}(E_\nu) + \phi_{\text{SPL}} \times \left(\frac{E_\nu}{100 \text{ TeV}}\right)^{-\gamma_{\text{SPL}}} \quad (6)$$

A representative set of different source-class specific predictions have been selected, focusing on predictions not already covered by the performed test of a single power law, and including variations of the benchmark models shown in the publications (see Table 6). All these predictions model the cumulative expected flux at Earth for the given source class. The obtained fit results using these predictions are listed in Table 6. The test statistic $TS_{\text{free model}}$ from Equation (7) compares the best-fit result including the additional component of the source-class specific flux prediction to the hypothesis of only a single power law. That is, $TS_{\text{free model}} = 0$ implies that the description of the experimental data can not be improved with an additional contribution from the model prediction and the fit instead prefers the single power-law model. For these cases, upper limits on the model normalization are computed at 90% CL employing Wilks’ theorem.

$$TS_{\text{free model}} = -2 \times \log \left(\frac{\mathcal{L}(D | \hat{\phi}_{\text{model}}, \hat{\phi}_{\text{SPL}}, \hat{\gamma}_{\text{SPL}}, \hat{\xi})}{\mathcal{L}(D | \phi_{\text{model}} \equiv 0.0, \phi_{\text{SPL}}, \gamma_{\text{SPL}}, \xi)} \right) \quad (7)$$

Similar to the results using the generic parameterizations for the energy spectrum, we find that model predictions with a softening of the spectral shape in the energy range 100 TeV – 1 PeV describe the experimental data better than the single power law. For example, the addition of spectral components as predicted by the models from Senno et al. (2016) and Liu et al. (2018)

Table 6
Results of the Likelihood Fits with an Additional Astrophysical Component following a Source-class Specific Flux Prediction

Model	Variation	$TS_{\text{free model}}$	ϕ_{model}	$\phi_{\text{astro}}^{\text{SPL}}$	γ^{SPL}	UL $\phi_{\text{model}}^{90\%}$
Biehl et al. (2018; GRB)	Sum model A	0.00	0.00	1.44	2.37	0.19
	Sum model B	0.00	0.00	1.44	2.37	4.92
Senno et al. (2015; SFG w. HNe)	Diffusion $\propto E^{\frac{1}{2}}$	-0.14	$0.12^{+0.27}_{-0.34}$	1.12	2.40	-
	Diffusion $\propto E^{\frac{1}{3}}$	-0.41	$0.23^{+0.29}_{-0.37}$	0.87	2.42	-
Murase et al. (2014; AGN inner Jets)	$\Gamma = 2.0$, Blazar	0.00	0.00	1.44	2.37	0.48
	$\Gamma = 2.0$, Torus	0.00	0.00	1.44	2.37	0.58
	$\Gamma = 2.3$, Blazar	0.00	0.00	1.44	2.37	0.48
	$\Gamma = 2.3$, Torus	0.00	0.00	1.44	2.37	0.27
Liu et al. (2018; AGN winds)	CR ($\Gamma = 2.1$)	-0.98	$0.87^{+0.49}_{-0.88}$	0.47	2.47	-
	CR ($\Gamma = 2.3$)	-4.12	$14.3^{+3.61}_{-5.97}$	0.12	2.04	-
Padovani et al. (2015; BL Lac)	$\frac{E_{\nu}}{E_{\gamma}} = 0.3$	0.00	0.00	1.44	2.37	0.27
	$\frac{E_{\nu}}{E_{\gamma}} = 0.8$	0.00	0.00	1.44	2.37	0.1
Kimura et al. (2015; lowL AGN)	Model B1	-1.69	$0.33^{+0.23}_{-0.25}$	0.89	2.46	-
	Model B4	0.00	0.00	1.44	2.37	0.24
Biehl et al. (2018; TDE)	No variations	0.00	0.00	1.44	2.37	0.63
Tavecchio & Ghisellini (2015; lowL BL Lac)	No variations	-1.74	$0.32^{+0.22}_{-0.24}$	0.82	2.47	-
Senno et al. (2016; GRB w. choked Jets)	No variations	-4.36	$2.6^{+0.4}_{-1.16}$	0.00	-	-

Note. The normalization is added as an additional fit parameter. A negative log-likelihood difference indicates that the data is better described with the additional component compared to the single power-law model. The last column shows the 90% CL (Wilks’ theorem) upper limit if the model normalization is fitted to zero. Tested source classes include different GRB and AGN scenarios, star-forming galaxies (SFG) with hypernovae (HNe), and TDEs. Low luminosity models are preceded by “lowL.”

($\Gamma = 2.3$) are favored compared to the pure single power-law hypothesis, with test statistics reaching $-TS_{\text{free model}} > 4$. For these two models, the best-fit model normalizations are multiples of the model prediction, substantially reducing the strength of the single power-law component, while neither model is claiming to account for the entire diffuse emission. When fixing the model normalization ($\Phi_{\text{model}} = 1.0$ in Equation (6)) and comparing to the single power-law model, only the models from Liu et al. (2018) and Senno et al. (2016) result in negative test statistics, indicating a small but insignificant preference of those model predictions Stettner (2021). For every other model in Table 6 which is yielding negative test statistics when allowing a free model normalization, the fitted normalization is smaller than the nominal prediction in the original publication.

Models in Table 6 predicting some spectral hardening in the considered energy range, like Biehl et al. (2018), Murase et al. (2014) and Padovani et al. (2015) are mildly disfavored. While this does not disfavor them as source models for individual neutrino sources, they are less likely to be main contributors to the overall diffuse astrophysical neutrino flux.

6. Discussion and Outlook

We have presented an updated measurement of the astrophysical muon-neutrino flux from the northern celestial sky. The last measurement from Aartsen et al. (2016) observed a flux compatible with a single power law described by a spectral index of $\gamma = 2.13^{+0.13}_{-0.13}$. Our update consists of more than three years of additional data (roughly doubling statistics), a re-processing of the full data with latest calibration and filtering standards (Pass-2) and an updated treatment of systematic uncertainties (detector effects and atmospheric fluxes). Assuming a single power-law energy spectrum, we find a spectral index of $2.37^{+0.09}_{-0.09}$. This is in agreement with but slightly softer than earlier iterations of this analysis. This change is partly caused by the updated atmospheric flux models

and uncertainty treatment but also by updated detector simulations of photon detection as well as the added data. In addition, we tested parameterizations beyond the single power law for the first time and find hints for a softening of the spectral shape as a function of energy at the two-sigma confidence level (cutoff, log-parabola, and piece-wise models). Figure 5 shows the result of the spectral fit in comparison to other measurements of the diffuse astrophysical flux by IceCube (Aartsen et al. 2019, 2020c; Abbasi et al. 2021) and the mild excess over expected atmospheric backgrounds observed by ANTARES (Fusco & Versari 2019). In the energy range where all referred analyses are sensitive, the observed event rates agree well with each other. The analyses themselves are based on event samples of varying statistical sizes, covering different energies and neutrino flavors. The advantages of the different analysis methods and the relations between the spectral results shown in Figure 5 are discussed in detail in Abbasi et al. (2021). With continued data taking of IceCube, it is expected that these measurements can be further improved in the future. Furthermore, with the future IceCube-Gen2 Observatory (Aartsen et al. 2021b), we expect a substantial increase of exposure by a factor of ≈ 6 , which will improve the statistics in the here probed energy range and also allow for extensions of the energy range to higher energies. A further goal of the collaboration is combining the measured astrophysical fluxes from different detection channels into a single consistent analysis based on a global fit of the data.

The IceCube collaboration acknowledges the significant contributions to this manuscript from Philipp Fürst, Jöran Stettner, and Christopher Wiebusch. We acknowledge the support from the following agencies: USA—U.S. National Science Foundation-Office of Polar Programs, U.S. National Science Foundation-Physics Division, U.S. National Science Foundation-EPSCoR, Wisconsin Alumni Research Foundation, Center for High Throughput Computing (CHTC) at the

Table 7
Table of Observed Events with $E_{\mu, \text{proxy}} > 200$ TeV, i.e., with a Signalness $S(E_{\mu}) = \frac{\Phi_{\text{signal}}(E_{\mu})}{\Phi_{\text{signal}}(E_{\mu}) + \Phi_{\text{background}}(E_{\mu})} \gtrsim 0.5$

ID	MJD	Energy (TeV)	Signalness	Decl. (deg)	R.A. (deg)	Δ_{Energy} (TeV)	$\Delta_{\text{Decl.}}$ (deg)	$\Delta_{\text{R.A.}}$ (deg)
I.4 ^a	55370.7	150	-110
I.6 ^b	55421.5
I.13 ^a	55722.4	180	-30
I.15 ^a	55896.9	110	-190
I.17 ^a	56063.0	180	-20
I.19 ^a	56211.8	200	-10
I.28 ^a	57049.5	190	-20
II.1 ^{IC59}	55056.7	480	0.78	1.23 ^{+0.18} _{-0.22}	29.51 ^{+0.40} _{-0.38}
II.2 ^{IC59}	55141.1	250	0.52	11.74 ^{+0.32} _{-0.38}	298.21 ^{+0.53} _{-0.57}
II.3	55355.5	350	0.72	22.63 ^{+2.72} _{-2.15}	346.29 ^{+2.11} _{-2.33}	10	-0.95	1.36
II.4	55387.5	200	0.53	21.22 ^{+2.53} _{-1.73}	307.31 ^{+2.77} _{-2.50}	-30	0.22	0.35
II.5	55464.9	390	0.74	13.48 ^{+0.32} _{-0.24}	266.26 ^{+0.55} _{-0.39}	-70	0.08	-0.03
II.6	55478.4	600	0.84	11.03 ^{+0.30} _{-0.36}	331.13 ^{+0.39} _{-0.48}	-60	-0.06	0.05
II.7	55497.3	850	0.88	0.34 ^{+0.16} _{-0.14}	88.86 ^{+0.29} _{-0.20}	-100	-0.16	-0.09
II.8	55513.6	460	0.79	3.17 ^{+0.31} _{-0.27}	285.56 ^{+0.48} _{-0.32}	-60	0.02	-0.39
II.9	55589.6	210	0.55	1.16 ^{+0.20} _{-0.29}	307.79 ^{+0.40} _{-0.51}	-30	0.13	0.08
II.10	55702.8	420	0.76	20.07 ^{+0.93} _{-0.93}	234.93 ^{+0.94} _{-0.98}	120	-0.23	-0.20
II.11	55764.2	220	0.56	6.02 ^{+6.77} _{-5.54}	315.53 ^{+2.47} _{-4.10}	10	0.73	-0.13
II.12	55911.3	630	0.84	18.49 ^{+1.80} _{-1.43}	36.56 ^{+1.29} _{-1.54}	-30	-0.61	-0.09
II.13	56146.2	250	0.59	1.60 ^{+0.23} _{-0.25}	329.68 ^{+0.47} _{-0.31}	-10	0.03	-0.42
II.14	56226.6	700	0.87	28.16 ^{+0.43} _{-0.60}	169.98 ^{+0.71} _{-0.96}	-50	0.12	0.37
II.15	56470.1	660	0.85	14.17 ^{+1.08} _{-0.87}	93.74 ^{+0.83} _{-1.01}	-10	-0.29	0.36
II.16	56521.8	420	0.76	-2.87 ^{+0.46} _{-0.52}	223.77 ^{+0.42} _{-0.45}	20	1.57	-1.12
II.17	56579.9	210	0.55	10.28 ^{+0.35} _{-0.46}	32.92 ^{+0.74} _{-0.57}	-180	0.08	-0.02
II.18	56666.5	830	0.88	33.02 ^{+0.39} _{-0.43}	293.12 ^{+0.67} _{-0.99}	-20	0.20	-0.17
II.19 ^c	56757.1	240	0.59	81.22 ^{+7.72} _{-5.86}	2.11 ^{+185.55} _{-47.87}	+160
II.20	56800.0	300	0.64	17.90 ^{+1.47} _{-1.12}	349.50 ^{+2.69} _{-2.69}	-100	-0.15	0.11
II.21	56817.6	340	0.70	1.31 ^{+0.84} _{-0.73}	106.26 ^{+2.20} _{-1.72}	0	0.02	-0.00
II.22	56819.2	4400	0.99	11.45 ^{+0.18} _{-0.15}	110.65 ^{+0.46} _{-0.58}	-100	0.03	0.02
II.23	57157.9	230	0.59	12.14 ^{+0.45} _{-0.43}	91.49 ^{+0.80} _{-0.63}	-10	-0.04	-0.11
II.24	57217.9	300	0.63	26.36 ^{+1.58} _{-1.81}	326.29 ^{+1.23} _{-1.08}	0	0.26	0.79
II.25	57246.8	370	0.73	6.17 ^{+0.42} _{-0.45}	328.27 ^{+0.61} _{-0.75}	-10	0.17	-0.13
II.26	57269.8	220	0.57	28.08 ^{+0.45} _{-0.42}	133.77 ^{+0.42} _{-0.71}	0	0.08	-0.23
II.27	57312.7	220	0.58	19.95 ^{+2.32} _{-1.94}	197.53 ^{+2.05} _{-2.08}	-10	0.05	-0.07
II.28	57340.9	730	0.87	12.71 ^{+0.56} _{-0.62}	76.16 ^{+1.15} _{-1.11}	-10	0.11	-0.14
II.29	57478.6	370	0.73	15.48 ^{+0.55} _{-0.64}	151.22 ^{+0.47} _{-0.53}	-10	-0.12	-0.11
II.30	57672.1	380	0.74	1.16 ^{+5.37} _{-2.60}	32.08 ^{+4.17} _{-4.41}	50	-25.44 ^d	22.38 ^d
II.31 ^e	57951.8	440	0.77	25.16 ^{+1.02} _{-1.15}	208.39 ^{+1.43} _{-0.98}
II.32 ^e	58063.8	1200	0.93	7.44 ^{+0.27} _{-0.24}	340.14 ^{+0.52} _{-0.53}
II.33 ^e	58141.7	290	0.62	8.61 ^{+0.57} _{-0.39}	76.33 ^{+1.88} _{-1.89}
II.34 ^e	58205.1	550	0.82	7.44 ^{+1.37} _{-1.27}	307.09 ^{+2.22} _{-4.00}
II.35 ^e	58264.3	390	0.74	8.27 ^{+1.49} _{-4.79}	210.67 ^{+5.56} _{-6.35}

Notes. The reconstructed muon energy is as used in the analysis (Abbasi et al. 2013). The directional reconstruction is based on a more sophisticated reconstruction algorithm that is also applied to real-time alerts (Aartsen et al. 2017c, 2018b). The given statistical uncertainty ranges are 90% CL, derived from reconstructions performed on a sample of similar events (Rädel 2017). See text for a description of the Pass-2 re-calibration campaign that leads to changes of reconstructed energy and direction for some events. Seven events that have been reported in the last publications (Aartsen et al. 2016; Haack & IceCube Collaboration 2018) are marked as dropped, either because their reconstructed energy falls below threshold or because they do not pass the event selection anymore.

^a Dropped: Pass-2 energy below threshold.

^b Dropped: Did not pass unified event selection.

^c New: Pass-2 energy above threshold.

^d Preliminary direction was reported in Aartsen et al. (2016).

^e New Event.

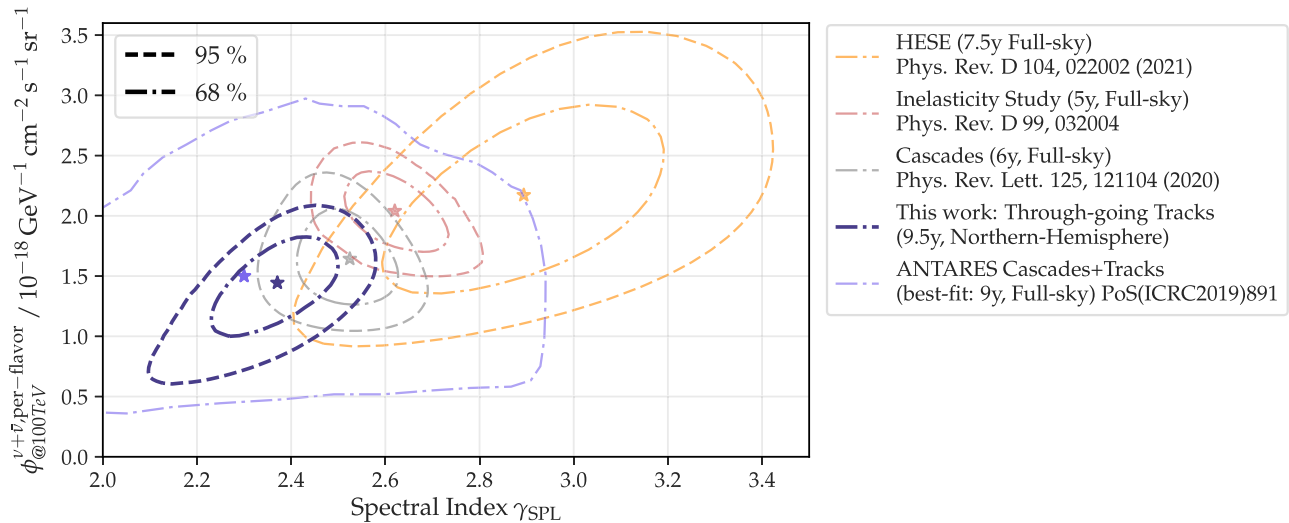


Figure 5. Summary of astrophysical neutrino flux measurements. Best-fit parameters and uncertainty contours for the single power-law hypothesis are drawn for studies based on high-energy starting events (Abbasi et al. 2021), cascade-like events (Aartsen et al. 2020c), and an inelasticity study (Aartsen et al. 2019) by IceCube. ANTARES observes a mild excess of events over the expected atmospheric backgrounds in a combined study of tracks and cascades (Fusco & Versari 2019).

University of Wisconsin-Madison, Open Science Grid (OSG), Extreme Science and Engineering Discovery Environment (XSEDE), Frontera computing project at the Texas Advanced Computing Center, U.S. Department of Energy-National Energy Research Scientific Computing Center, Particle astrophysics research computing center at the University of Maryland, Institute for Cyber-Enabled Research at Michigan State University, and Astroparticle physics computational facility at Marquette University; Belgium—Funds for Scientific Research (FRS-FNRS and FWO), FWO Odysseus and Big Science programmes, and Belgian Federal Science Policy Office (Belspo); Germany—Bundesministerium für Bildung und Forschung (BMBF), Deutsche Forschungsgemeinschaft (DFG), Helmholtz Alliance for Astroparticle Physics (HAP), Initiative and Networking Fund of the Helmholtz Association, Deutsches Elektronen Synchrotron (DESY), and High Performance Computing cluster of the RWTH Aachen; Sweden—Swedish Research Council, Swedish Polar Research Secretariat, Swedish National Infrastructure for Computing (SNIC), and Knut and Alice Wallenberg Foundation; Australia—Australian Research Council; Canada—Natural Sciences and Engineering Research Council of Canada, Calcul Québec, Compute Ontario, Canada Foundation for Innovation, West-Grid, and Compute Canada; Denmark—Villum Fonden and Carlsberg Foundation; New Zealand—Marsden Fund; Japan—Japan Society for Promotion of Science (JSPS) and Institute for Global Prominent Research (IGPR) of Chiba University; Korea—National Research Foundation of Korea (NRF); Switzerland—Swiss National Science Foundation (SNSF); United Kingdom—Department of Physics, University of Oxford.

Appendix A Supplementary Material

A.1. Barr Treatment of Atmospheric Uncertainties

The nuisance parameters are included in the fit to cover the systematic uncertainties affecting this measurement, with the goal of measuring an unbiased result. The scheme from Barr et al. (2006) was adopted to cover atmospheric flux uncertainties. Previous analyses used a parameter describing the ratio between the integrated neutrino fluxes arising from kaon and pion decays, respectively (Aartsen et al. 2016; Haack & IceCube Collaboration 2018). In principle, the Barr scheme allows for an uncertainty in the production yield of each individual meson, for example pions and antipions. Different from a global scaling of these production yields, each parameter describes uncertainties in a specific region of meson production phase space, with the goal of having different parameters for regions dominated by different physical effects and with different experimental coverage. Since the total $\nu + \bar{\nu}$ flux is measured in this analysis, the parameters for mesons and antimessons can be combined into single parameters here. Flux gradients are then calculated from flux predictions obtained with different parameter values, and the Barr parameters in the fit then scale this gradient to obtain a flux prediction depending on parameter value. Since they affect the neutrino production, the Barr parameters are correlated to the absolute normalization of the conventional atmospheric flux, but crucially also introduce energy-dependent flux variations (Stettner 2021). The correlations between the nuisance parameters are shown in Figure 6.

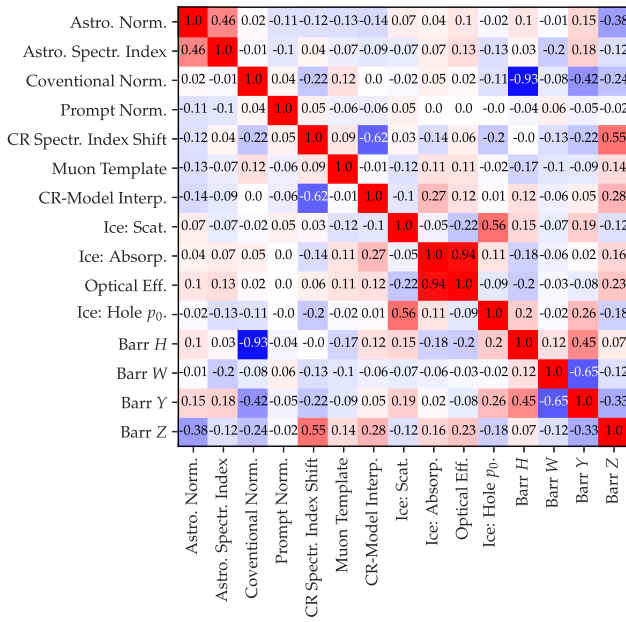


Figure 6. Pearson correlation coefficients between the signal and nuisance parameters are shown for the parameters of the single power-law fit.

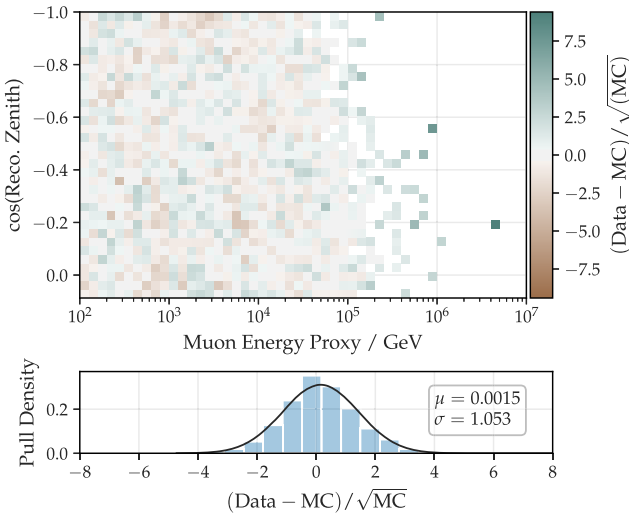


Figure 7. The upper figure shows the statistical pull per bin between the experimental data and the MC expectation assuming the best-fit energy spectrum obtained in Section 4. The lower figure shows the pull density distribution for the 1048 analysis bins containing data events.

A.2. Correlation Coefficients

The Pearson correlation coefficients between signal and nuisance parameters are calculated and shown in Figure 6

A.3. Pull Density Distribution

The per-bin difference between experimental data and MC expectation is shown in Figure 7, which shows the statistical pull per bin in the upper part and the respective pull distribution in the lower part.

ORCID iDs

R. Abbasi <https://orcid.org/0000-0001-6141-4205>
M. Ackermann <https://orcid.org/0000-0001-8952-588X>

J. A. Aguilar <https://orcid.org/0000-0003-2252-9514>
M. Ahlers <https://orcid.org/0000-0003-0709-5631>
J. M. Alameddine <https://orcid.org/0000-0002-9534-9189>
G. Anton <https://orcid.org/0000-0003-2039-4724>
C. Argüelles <https://orcid.org/0000-0003-4186-4182>
A. Balagopal V. <https://orcid.org/0000-0001-5367-8876>
A. Barbano <https://orcid.org/0000-0002-4836-7093>
S. W. Barwick <https://orcid.org/0000-0003-2050-6714>
V. Basu <https://orcid.org/0000-0002-9528-2009>
S. Baur <https://orcid.org/0000-0002-3329-1276>
J. J. Beatty <https://orcid.org/0000-0003-0481-4952>
K.-H. Becker <https://orcid.org/0000-0002-1748-7367>
S. BenZvi <https://orcid.org/0000-0001-5537-4710>
E. Bernardini <https://orcid.org/0000-0003-3108-1141>
E. Blauffuss <https://orcid.org/0000-0001-5450-1757>
S. Blot <https://orcid.org/0000-0003-1089-3001>
S. Böser <https://orcid.org/0000-0002-5918-4890>
O. Botner <https://orcid.org/0000-0001-8588-7306>
F. Bradascio <https://orcid.org/0000-0002-7750-5256>
A. Burgman <https://orcid.org/0000-0003-1276-676X>
M. A. Campana <https://orcid.org/0000-0003-4162-5739>
C. Chen <https://orcid.org/0000-0002-8139-4106>
D. Chirkin <https://orcid.org/0000-0003-4911-1345>
B. A. Clark <https://orcid.org/0000-0003-4089-2245>
K. Clark <https://orcid.org/0000-0003-2467-6825>
A. Coleman <https://orcid.org/0000-0003-1510-1712>
J. M. Conrad <https://orcid.org/0000-0002-6393-0438>
P. Coppin <https://orcid.org/0000-0001-6869-1280>
P. Correa <https://orcid.org/0000-0002-1158-6735>
R. Cross <https://orcid.org/0000-0003-0081-8024>
P. Dave <https://orcid.org/0000-0002-3879-5115>
C. De Clercq <https://orcid.org/0000-0001-5266-7059>
J. J. DeLaunay <https://orcid.org/0000-0001-5229-1995>
D. Delgado López <https://orcid.org/0000-0002-4306-8828>
H. Dembinski <https://orcid.org/0000-0003-3337-3850>
A. Desai <https://orcid.org/0000-0001-7405-9994>
P. Desiati <https://orcid.org/0000-0001-9768-1858>
K. D. de Vries <https://orcid.org/0000-0002-9842-4068>
G. de Wasseige <https://orcid.org/0000-0002-1010-5100>
T. DeYoung <https://orcid.org/0000-0003-4873-3783>
A. Diaz <https://orcid.org/0000-0001-7206-8336>
J. C. Díaz-Vélez <https://orcid.org/0000-0002-0087-0693>
H. Dujmovic <https://orcid.org/0000-0003-1891-0718>
M. A. DuVernois <https://orcid.org/0000-0002-2987-9691>
P. Eller <https://orcid.org/0000-0001-6354-5209>
A. R. Fazely <https://orcid.org/0000-0002-6907-8020>
C. Finley <https://orcid.org/0000-0003-3350-390X>
D. Fox <https://orcid.org/0000-0002-3714-672X>
A. Franckowiak <https://orcid.org/0000-0002-5605-2219>
P. Fürst <https://orcid.org/0000-0002-7951-8042>
T. K. Gaisser <https://orcid.org/0000-0003-4717-6620>
E. Ganster <https://orcid.org/0000-0003-4393-6944>
A. Garcia <https://orcid.org/0000-0002-8186-2459>
S. Garrappa <https://orcid.org/0000-0003-2403-4582>
A. Ghadimi <https://orcid.org/0000-0002-6350-6485>
T. Glauch <https://orcid.org/0000-0003-1804-4055>
T. Glüsenskamp <https://orcid.org/0000-0002-2268-9297>
S. Griswold <https://orcid.org/0000-0002-7321-7513>
P. Gutjahr <https://orcid.org/0000-0001-7980-7285>
A. Hallgren <https://orcid.org/0000-0001-7751-4489>
L. Halve <https://orcid.org/0000-0003-2237-6714>
F. Halzen <https://orcid.org/0000-0001-6224-2417>
A. Haungs <https://orcid.org/0000-0002-9638-7574>

- Aartsen, M., Ackermann, M., Adams, J., et al. 2018a, *Sci*, **361**, 147
- Aartsen, M., Ackermann, M., Adams, J., et al. 2020a, *PhRvL*, **124**, 051103
- Aartsen, M., Ackermann, M., Adams, J., et al. 2020b, *JInst*, **15**, P06032
- Aartsen, M. G., Abbasi, R., Abdou, Y., et al. 2013, *PhRvL*, **111**, 021103
- Aartsen, M. G., Ackermann, M., Adams, J., et al. 2017d, *ApJ*, **843**, 112
- Aartsen, M. G., Ackermann, M., Adams, J., et al. 2018b, *Sci*, **361**, 6398
- Aartsen, M. G., Ackermann, M., Adams, J., et al. 2019, *PhRvD*, **99**, 032004
- Aartsen, M. G., Ackermann, M., Adams, J., et al. 2020c, *PhRvL*, **125**, 121104
- Abbasi, R., Abdou, Y., Abu-Zayyad, T., et al. 2010, *NIMPA*, **618**, 139
- Abbasi, R., Abdou, Y., Abu-Zayyad, T., et al. 2012a, *Natur*, **484**, 351
- Abbasi, R., Abdou, Y., Abu-Zayyad, T., et al. 2012b, *APh*, **35**, 615
- Abbasi, R., Abdou, Y., Ackermann, M., et al. 2013, *NIMPA*, **703**, 190
- Abbasi, R., Ackermann, M., Adams, J., et al. 2009, *NIMPA*, **601**, 294
- Abbasi, R., Ackermann, M., Adams, J., et al. 2021, *PhRvD*, **104**, 022002
- Ahlers, M., & Halzen, F. 2018, *PrPNP*, **102**, 73
- Ahrens, J., Bai, X., Bay, R., et al. 2004, *NIMPA*, **524**, 169
- Barr, G. D., Robbins, S., Gaisser, T. K., & Stanev, T. 2006, *PhRvD*, **74**, 094009
- Becker, J. K. 2008, *PhR*, **458**, 173
- Becker Tjus, J., & Merten, L. 2020, *PhR*, **872**, 1
- Bhattacharya, A., Enberg, R., Reno, M. H., Sarcevic, I., & Stasto, A. 2015, *JHEP*, **2015**, 110
- Biehl, D., Boncioli, D., Fedynitch, A., & Winter, W. 2018, *A&A*, **611**, A101
- Biehl, D., Boncioli, D., Lunardini, C., & Winter, W. 2018, *NatSR*, **8**, 10828
- Chirkin, D. 2015, *GPU Computing in High-Energy Physics*, DESY-PROC-2014-05
- Chirkin, D., Díaz-Vélez, J. C., Kopper, C., et al. 2019, 2019 15th International Conference on eScience (eScience) (San Diego, CA: IEEE)
- Cooper-Sarkar, A., Mertsch, P., & Sarkar, S. 2011, *JHEP*, **2011**, 42
- Dai, L., & Fang, K. 2017, *MNRAS*, **469**, 1354
- Eller, P. 2019, Unified Hole-ice Model: Angular-acceptance Code, GitHub, https://github.com/philippeller/angular_acceptance
- Enberg, R., Reno, M. H., & Sarcevic, I. 2008, *PhRvD*, **78**, 043005
- Farrar, G. R., & Piran, T. 2014, arXiv:1411.0704
- Fedynitch, A., Engel, R., Gaisser, T. K., Riehn, F., & Stanev, T. 2015, in *ISVHECRI 2014 – 18th Int. Symp. on Very High Energy Cosmic Ray Interactions*, 99, ed. D. Berge et al., 08001
- Fedynitch, A., Riehn, F., Engel, R., Gaisser, T. K., & Stanev, T. 2019, *PhRvD*, **100**, 103018
- Fusco, L. A., & Versari, F. 2019, ICRC (Madison, WI), 358, 891
- Gaisser, T. K. 2012, *Aph*, **35**, 801
- Gaisser, T. K., Stanev, T., & Tilav, S. 2013, *FrPhy*, **8**, 748
- Guépin, C., & Kotera, K. 2017, *A&A*, **603**, A76
- Haack, C., Wiebusch, C. & (IceCube Collaboration) 2018, *ICRC (Busan)*, 301, 1005
- Halzen, F., & Klein, S. R. 2010, *RSci*, **81**, 081101
- Hayasaki, K. 2021, *NatAs*, **5**, 436
- Heck, D., Knapp, J., Capdevielle, J., et al. 1998, Karlsruhe, Forschungszentrum, Technical Report, FZKA-6019 6019
- Honda, M., Kajita, T., Kasahara, K., Midorikawa, S., & Sanuki, T. 2007, *PhRvD*, **75**, 043006
- Köhne, J. H., Frantzen, K., Schmitz, M., et al. 2013, *CoPhC*, **184**, 2070
- Kimura, S. S., Murase, K., & Toma, K. 2015, *ApJ*, **806**, 159
- Learned, J. G., & Mannheim, K. 2000, *ARNPS*, **50**, 679
- Liu, R.-Y., Murase, K., Inoue, S., Ge, C., & Wang, X.-Y. 2018, *ApJ*, **858**, 9
- Loeb, A., & Waxman, E. 2006, *JCAP*, **05**, 003
- Lunardini, C., & Winter, W. 2017, *PhRvD*, **95**, 123001
- Murase, K., Inoue, Y., & Dermer, C. D. 2014, *PhRvD*, **90**, 023007
- Padovani, P., Petropoulou, M., Giommi, P., & Resconi, E. 2015, *MNRAS*, **452**, 1877
- Rädel, L. 2017, PhD thesis, RWTH Aachen Univ., <http://publications.rwth-aachen.de/record/709576>
- Rongen, M. 2019, PhD thesis, RWTH Aachen Univ., <http://publications.rwth-aachen.de/record/771097>
- Schatto, K. 2014, PhD thesis, Johannes Gutenberg-Universität Mainz, <https://opencience.ub.uni-mainz.de/handle/20.500.12030/2899>
- Senno, N., Mészáros, P., Murase, K., Baerwald, P., & Rees, M. J. 2015, *ApJ*, **806**, 24
- Senno, N., Murase, K., & Meszaros, P. 2016, *PhRvD*, **93**, 083003
- Senno, N., Murase, K., & Mészáros, P. 2017, *ApJ*, **838**, 3
- Stein, R., Velzen, S. v., Kowalski, M., et al. 2021, *NatAs*, **5**, 510
- Stettner, J. & IceCube Collaboration 2019, ICRC (Madison, WI), **36**, 1017
- Stettner, J. B. 2021, PhD thesis, RWTH Aachen Univ. <https://publications.rwth-aachen.de/record/811376>
- Tamborra, I., Ando, S., & Murase, K. 2014, *JCAP*, **09**, 043
- Tavecchio, F., & Ghisellini, G. 2015, *MNRAS*, **451**, 1502
- Wilks, S. S. 1938, *Ann. Math. Statist.*, **9**, 60